



Precipitation Behavior of Carbide and its Effect on the Mechanical Properties of a Novel $\text{Fe}_{60}\text{Co}_{10}\text{Cr}_{10}\text{Ni}_{10}\text{Mo}_5\text{V}_5$ Medium-Entropy Alloy

HEBIN WANG,¹ DA HONG,¹ LONGGANG HOU,^{2,3} PING OU,¹
LI SHEN,¹ YIQI WANG,¹ ZHIGANG WANG,¹ and HONGJIN ZHAO^{1,4}

1.—School of Materials Science and Engineering, Jiangxi University of Science and Technology, Ganzhou 341000, China. 2.—State Key Laboratory for Advanced Metals and Materials, University of Science and Technology Beijing, Beijing 100083, China. 3.—e-mail: lghou@skl.ustb.edu.cn. 4.—e-mail: zhj_zyh@163.com

Carbide precipitates are effective for improving the strength and stability of high-entropy alloys. In this work, novel-designed $\text{Fe}_{60}\text{Co}_{10}\text{Cr}_{10}\text{Ni}_{10}\text{Mo}_5\text{V}_5$ medium-entropy alloys (MEAs) containing 1 wt.% carbon were prepared by vacuum arc melting followed by solid solution treatment and aging. The effects of aging on the microstructure and mechanical properties of the MEAs were investigated. The results showed that the microstructure of the solution-treated alloy was comprised of the face-centered cubic (FCC) matrix, coarse $\text{M}_2\text{C}/\text{MC}$ carbides, and tiny fine undissolved MC precipitates distributed on the grain boundaries and inside the grains. A high number density of cube-shaped MC precipitates, with an approximate mean size of 24 nm precipitate within the FCC matrix in the case of aging at 800°C for 2 h, contribute to the highest hardness and tensile strength of the sample without sacrificing its elongation. With increasing aging temperature and time, the size of the MC precipitates increased while their volume fraction decreased. The strengthening effect can be attributed to the combination of the precipitation strengthening and solid solution strengthening.

INTRODUCTION

High-entropy alloys (HEAs), which were first proposed by Yeh¹ and Cantor² in 2004, are alloys comprised of five or more principle elements with nearly equal proportions, for which the high entropy of mixing favors the formation of simple solid solutions face-centered cubic (FCC),^{3–8} body-centered cubic,^{9–13} or hexagonal close-packed structures (HCP).^{14–16} This novel alloy design strategy is quite different from the conventional alloy design concept that usually starts with one or two elements as the main components and adds other minor elements to obtain improved properties. Because of the several unique intrinsic characteristics, such as high configuration entropy, sluggish diffusion, and severe lattice distortion of HEAs, they usually display a combination of superior mechanical

properties, good corrosion resistance, and high-temperature stability. As a typical FCC single phase alloy, CoCrFeNi is one of the widely reported HEAs with excellent ductility.¹⁷ However, for practical applications, the strength of this alloy with the FCC matrix alone is generally insufficient. In other words, some strengthening mechanisms must be introduced to attain desirable mechanical properties.

Precipitation hardening has been suggested to be an effective approach for the strengthening of HEAs. A combination of substantially increased strength without a high sacrifice of ductility was observed for CoCrFeNi HEAs with the alloying addition of Mo, which induced the precipitation of hard σ and μ intermetallics in the FCC matrix.¹⁸ He et al.¹⁹ reported on the strengthening of FCC-CoCrFeNi HEAs by nanosized coherent L_{12} particles using an addition of small amounts of Ti and Al, which achieved a high tensile strength of 1273 MPa

and a good ductility of 17%; however, some large L2₁ Heusler particles appeared in this alloy which degraded its toughness. Other investigations²⁰ also revealed the strengthening of the Nb-rich Laves phase in CoCrFeNiNb_x HEAs, but the precipitates were unevenly distributed irregular compounds with a size of several microns, giving rise to improved strength but a remarkable decrease in plasticity. Recently, precipitation strengthening by carbide phases or interstitial strengthening by carbon has provided another approach to improve the strength of HEAs. For example, nano-sized Cr₂₃C₆ precipitates were distributed on the grain boundaries and cell structures in an annealed FeCoCrNiC_{0.05} HEA, leading to an increase in strength but a decrease in elongation.²¹ Gao et al.²² introduced 0.8 at.% Nb and C into CrMnFeCoNi-based HEAs, which resulted in an enhanced tensile strength of 911 MPa while maintaining a good elongation of 32%, and the abundant fine NbC precipitates inside the grains were the main origin of the substantial improvements in the properties. In particular, carbide precipitates such as VC, NbC, and Mo₂C that have been widely applied in steel are very close to the ideal secondary phases that contribute to the remarkable strengthening effect.^{23–25} However, the relationships between the carbide precipitates and the mechanical properties of HEAs are still unclear.

Recently, many studies have concluded that the equiatomic composition is not a necessary condition for the formation of a complete solid solution in HEAs. For example, a single FCC phase was obtained in non-equiatomic Fe₄₀Co₅Cr₂Mn₂₇Ni₂₆ HEA.²⁶ Li et al.²⁷ found that Fe_{80-x}Mn_xCo₁₀Cr₁₀ HEAs exhibited a single FCC phase when the concentration of Mn was 40 at.% or 45 at.%. Bae et al.²⁸ investigated Fe_x(CoNi)_{90-x}Cr₁₀ HEAs with the Fe content ranging from 55 at.% to 60 at.% and found that all these alloys were composed of a single FCC phase. These results indicate that the ranges of the chemical composition for single FCC phase HEAs can be widened to go beyond the traditional equiatomic CoCrFeNi HEA systems. Therefore, we designed a non-equiatomic Fe₆₀Co₁₀Cr₁₀Ni₁₀Mo₅V₅ HEA with a heavy carbon addition in order to form abundant nanoscale carbide precipitates in the FCC matrix. This alloy can be regarded as a medium-entropy alloy (MEA) according to the entropy-based definition that defines MEAs as alloys with a configuration entropy between R and 1.5 R, and which can act as a bridge between HEAs and high-alloy steels.

In this study, we investigated the precipitation behavior of carbides and its effect on the mechanical properties of a novel Fe₆₀Co₁₀Cr₁₀Ni₁₀Mo₅V₅ MEA. The microstructure evolution and age-hardening phenomena of this alloy were analyzed, and the corresponding strengthening mechanisms are discussed.

MATERIALS AND METHODS

An alloy, based on the Fe₆₀Co₁₀Cr₁₀Ni₁₀Mo₅V₅ MEA doped with 1 wt.% carbon, was produced by arc-melting a mixture of pure metals, Fe, Co, Cr, Ni, Mo, V (purity > 99.9%), and Fe–C master alloy (5 wt.%C) under a high-purity argon atmosphere. The resulting ingot with the dimensions of approximately Φ 30 mm \times 120 mm was flipped and remelted five times in order to ensure the homogeneity of the chemical composition. To decrease the degree of segregation and dissolve the alloying elements as much as possible prior to aging, samples cut from the ingot were first solid solution-treated at 1453 K for 1 h followed by quenching in water, based on the heat treatment systems of high-alloy steel for which the microstructure is mainly composed of large amount of carbides. After solid-solution treatment, the specimens were aged for 0.5–12 h at 400–1100°C.

For metallographic examination, the specimens were prepared by mechanical grinding with SiC paper followed by electro-polishing in a solution of 20% perchloric acid, 10% glycerol, and 70% ethanol with a voltage of 20 V. The phase constitutions were identified using an x-ray diffractometer (Bruker D8-Advance, Germany) with Cu K_α radiation at 12 KW, a 2 θ range of 20°–90°, a step size of 0.02° and a scanning speed of 4°/min. The structures were examined using x-ray diffraction (XRD) and characterized using a Zeiss Sigma scanning electron microscope (SEM; Zeiss, Germany) and a FEI Tecnai G2 F20 transmission electron microscope (TEM; FEI, USA) equipped with an energy dispersive spectrometer (EDX). Thin foils for the TEM observation were prepared by twin-jet electropolishing, using a solution composed of 10% perchloric acid and 90% glacial acetic acid at –10°C with a supply voltage of 45 V and a current of 30 mA. The average precipitate diameter, d , was calculated from the precipitate size distributions using the image analysis software (Image-Pro Plus; Media Cybernetics, USA). The precipitate volume fraction (f) was estimated as $f = A_f$, where A_f is the projected area fraction of the precipitates. Five SEM images of each sample were taken at a magnification of \times 80,000 for different states. The total number of particles measured ranged from approximately 300–1500, depending on the aging temperature and time.

For all the samples, the sample (10 \times 10 \times 5 mm) hardness was determined using a Vickers hardness tester with a load of 1 kg and dwell time of 15 s, and ten measurements were performed to obtain the average value in order to decrease the experimental errors. Tensile tests were performed using a UTM5105 tension machine at room temperature with an engineering strain rate of $1 \times 10^{-3} \text{ s}^{-1}$. Flat dog-bone-shaped tensile specimens with a gauge length of 10 mm, width of 3 mm, and thickness of 1 mm were carefully ground using 2000-grit SiC

paper. The strains of the samples were measured by a DIC strain measurement system during the tensile tests. To ensure repeatability, three specimens were tested for each alloy.

RESULTS AND DISCUSSION

Phase Constituents and Age-Hardening Curves

Figure 1 shows the XRD patterns of the investigated alloys after the solution treatment and aging at different conditions. The solution-treated MEA consisted of an FCC solid solution matrix (JCPDS card #31-0619), a second FCC-type MC (JCPDS card #65-8074), and HCP-type M_2C (JCPDS card #35-0787), where M represented the multi-component mixture of the alloying elements such as Mo, V, Cr, and Fe. When the alloy was aged at 600°C for 4 h, the alloy retained the same phase composition as that of the solid solution state, and no other phase was detected within the limitation of the XRD detector. However, for the aging temperatures between 800 and 1000°C, the (200) and (220) peaks of the FCC phase were found to clearly shift to the higher 2θ , indicating that some fine secondary phases may have precipitated from the FCC matrix and decreased its lattice constant. The change in the lattice constants of the FCC phases in different states verify this result because the lattice parameter of the FCC phase was measured to be approximately 0.3602 nm after solution treatment, and this value decreased to 0.3584 nm and 0.3589 nm after aging at 800°C for 2 h and 12 h, respectively.

Figure 2a shows the influence of the aging temperatures on the hardness of the investigated alloy. The hardness of the alloy in the solid solution state was 220 HV, and a substantial hardening effect was observed for the alloy aging from 400°C to 800°C. The maximum hardness appeared at 800°C and was 352 HV. Then, the hardening effect decreased with the further increase in the temperature. It can be noted that no obvious softening compared to the hardness of the solution treated alloy occurred even after aging at a temperature up to 1100°C. Figure 2b illustrates the hardness variation of the alloy aged at 800°C as a function of time. The hardness clearly increased in the first 2 h, and reached the highest value of 365 HV. A further increase in the aging time to 4 h resulted in a slight decrease in the hardness to 350 HV. Further increase in the aging time led to gradual softening. Nevertheless, the hardness of the alloy aged at 800°C for 12 h was still substantially higher than that in the solid solution state (320 HV vs. 220 HV).

Microstructures

To elucidate the origin of the hardening of the alloy after aging, an investigation was carried out on the microstructure. The SEM image of the investigated alloy after the solution treatment

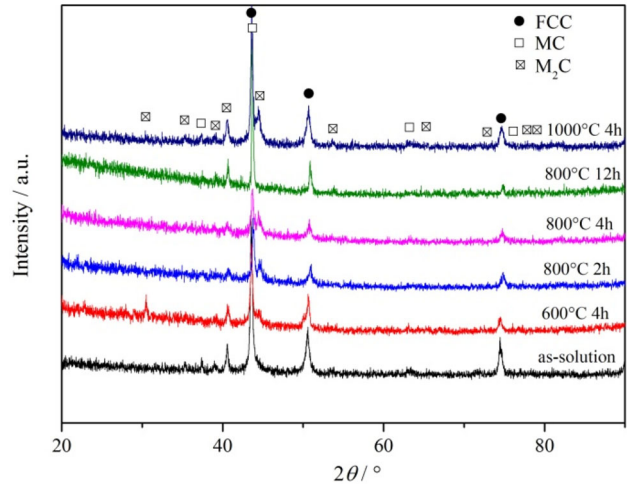


Fig. 1. XRD patterns of the alloy after solution treatment and aging in different conditions.

revealed a typical dendritic structure with a number of second chrysanthemum phases distributed in the interdendritic regions (Fig. 3a). According to the phase diffraction peaks of the XRD pattern in Fig. 1 and the results of the EDX analysis shown in Table S1, the dendritic structure is the FCC matrix for which the composition is almost the same as the alloy composition but with reduced Mo and V content. The interdendritic region consists of M_2C enriched with Mo, Cr, and a small amount of V-rich MC carbides. Additionally, some fine individual particles with the dimensions of approximately 50–200 nm are also observed inside the grains. A more detailed TEM study unambiguously shows that these precipitates are of the cubic MC-type (Fig. 3b), indicating that the concentration of the V element dissolved in the matrix after the solution treatment exceeds the solid solubility limit of the FCC phase, so that some of the excess MC precipitates remain. The microstructure of the alloy aged at 600°C for 4 h is similar to that of the solution-treated alloy, and no phases other than undissolved MC particles are detected (Fig. 3c). When the alloy is aged at 800°C for 2 h, corresponding to the conditions of maximum hardening, an abundance of fine secondary precipitates with estimated sizes ranging from a few to a dozen nanometers are found to be distributed uniformly in the matrix (Fig. 3d). These precipitates are identified as FCC-type MC carbides by electron diffraction (Fig. 4), and are thought to be responsible for the optimal age hardening that occurs at 800°C. Additionally, some coarse MC carbides with dimensions of 50–150 nm are also observed, and are surrounded by fine MC precipitates, indicating that some of these dense precipitates may become agglomerated into larger MC particles during their growth. As shown in Fig. 3e, an increase in the aging time to 4 h causes these fine MC precipitates to agglomerate further to form a homogeneous population of particles

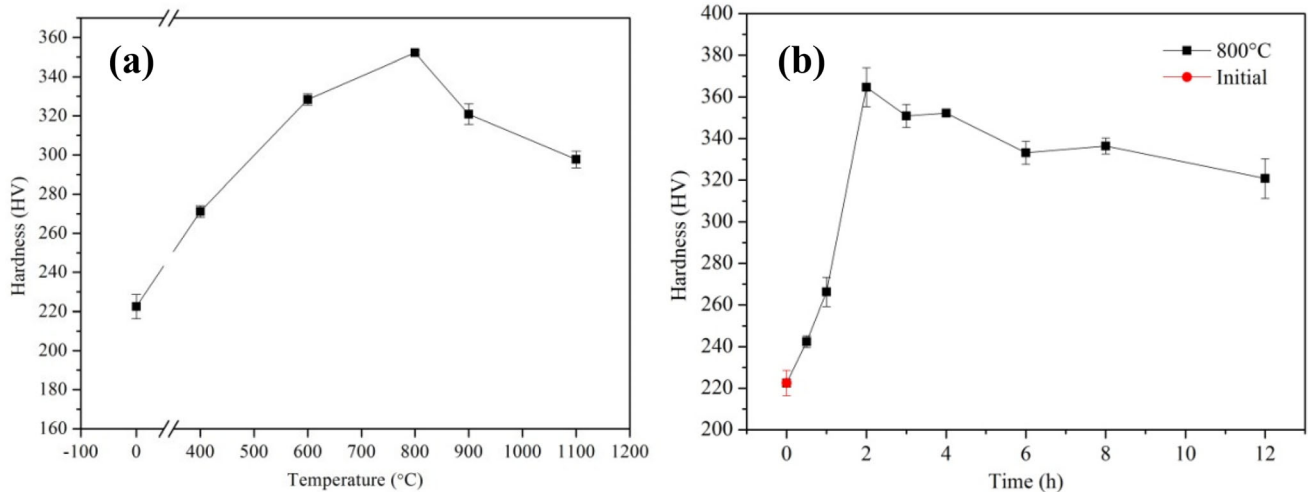


Fig. 2. Hardness values of the aged alloy for aging at different temperatures (a) and for different aging time at 800°C (b).

throughout the FCC matrix. An examination of the magnified view of the SEM image (Fig. 3f) shows that these particles are composed of round or square MC particles with diameters of approximately 70 nm and fine MC precipitates with a size of approximately 15 nm. The particles are clearly coarser compared to those in the alloy aged for 2 h. A further increase in the temperature to 1000°C leads to the coarsening of the precipitates, as shown in Fig. 3g and h, and the number density of the fine MC precipitates decreases remarkably with the increase in the average size, which is measured to be in the range of approximately 45–150 nm. Meanwhile, some coarse MC are found to agglomerate and restack into a strip structure (Fig. 3h). A comparison of the size and distribution of the precipitates in different states of aging indicates that, with increasing aging time and temperature, the age hardening precipitates in the FCC matrix become less dispersed and coarsened, decreasing the hardness.

Figure 4 shows TEM micrographs of the sample after aging at 800°C for 2 h and 12 h. An abundance of cube-shaped precipitates with sizes of 5–10 nm are observed in the matrix (Fig. 4a and b). The corresponding selected area diffraction pattern confirmed that these particles were MC-type particles (Fig. 4c). As the tempering time increased to 12 h, some MC precipitates with a size of approximately 30 nm were observed, indicating that the sizes of the fine precipitates were slightly higher than those of the 2-h aged specimen (Fig. 4d). Note that the MC precipitates showed the characteristic appearance of Moiré fringes, and that the Moiré fringes were parallel to the (11-1) planes of the FCC matrix. The additional satellite spots around the reflections of the MC phase and the FCC matrix in the selected area diffraction pattern arise from the Moiré fringes, as shown in Fig. 4e. Figure 4f shows the inverse fast Fourier transformation (IFFT) image of

the MC precipitates marked by a rectangle in Fig. 4d, and it is clear from an inspection of the figure that numerous MC carbides with the morphology of Moiré fringes are densely distributed in the matrix. The fringe spacing is approximately 1.6470 nm, which is consistent with the value calculated as $1/\Delta g$, where $\Delta g = g(11-1)_\gamma - g(11-1)_{\text{MC}}$. This indicates that the Moiré fringe is due to the interference between the (11-1) reflections of the MC phase and the FCC matrix.²⁹ Based on the above analysis, it is concluded that the fine precipitates are the MC phase and the lattice of the MC precipitates is oriented with respect to the FCC matrix according to a cube-on-cube orientation relationship. The typical EDX spectra shown in Fig. 4g obtained from the precipitate indicate that the cube-shaped precipitate contain a large proportion of V and a certain amount of Mo and Cr. These results further confirm that the precipitate is a V-rich MC phase. Moreover, from the TEM observation, it is found that MC carbides precipitate mainly on the dislocations. This can be attributed to the fact that small interstitial C atoms tend to diffuse to the dislocation cores during high-temperature aging, and that the precipitates can easily nucleate on these sites.

Mechanical Properties

Typical tensile engineering stress–strain diagrams of the solution MEA and aged MEA (800°C for 2 h and 4 h) are shown in Fig. 5a. The yield strength (YS), ultimate strength (UTS), and elongation of the as-solution treated MEA are 236 MPa, 475 MPa, and 2.5% (plastic strain 2.47%), respectively. In contrast, the 800°C/2 h aged alloy exhibits a high YS and UTS of 485 MPa and 668 MPa, respectively. With the aging time increasing to 4 h, the MEA values show a slight decrease (YS = 339 MPa and UTS = 597 MPa). For the 1000°C/4 h aged alloy, the MEA YS and UTS decrease to 271 MPa

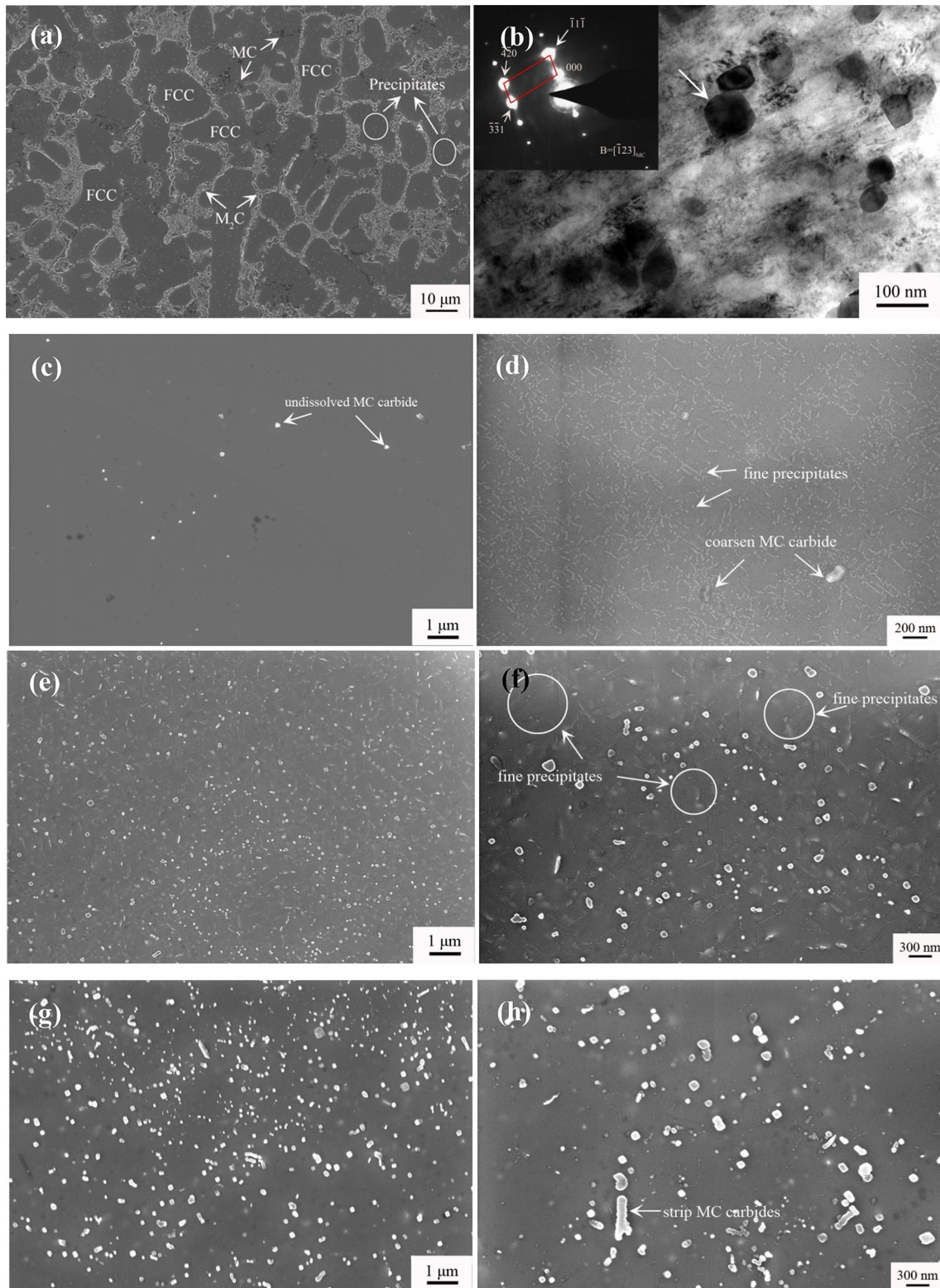
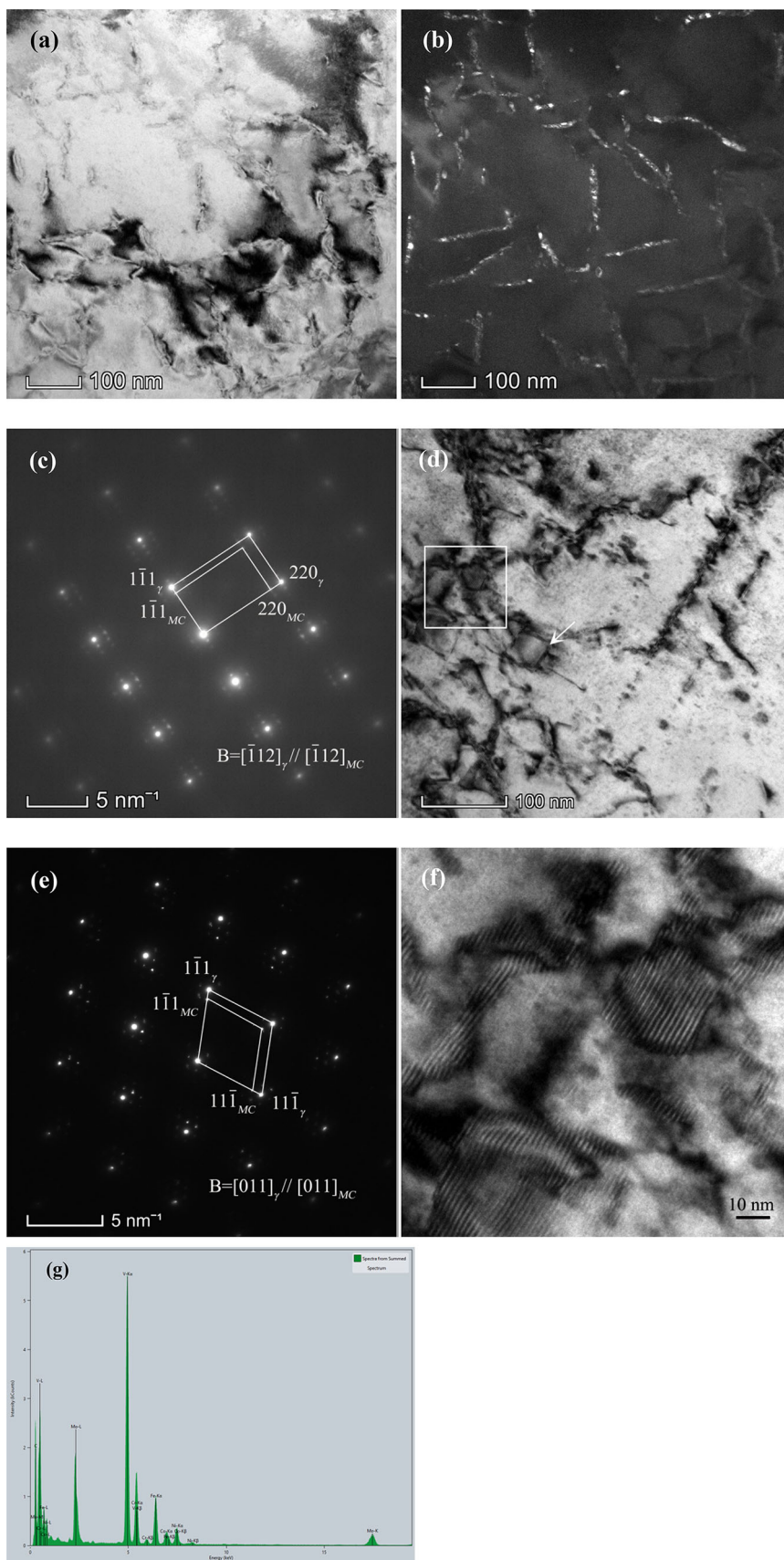


Fig. 3. Microstructures of the solution-treated and aged alloys: (a, b) solution-treated; (c) 600°C for 4 h; (d) 800°C for 2 h; (e, f) 800°C for 4 h; and (g, h) 1000°C for 4 h.



◀ Fig. 4. TEM micrographs of the MC precipitates in the sample aged at 800°C for 2 h (a–c) and 12 h (d–f): (a) bright field; (b) dark field; (c) selected area diffraction pattern; (d) bright field; (e) selected area diffraction pattern; (f) IFFT image of the rectangle marked in (d); and (g) EDX spectra of MC carbides indicated by arrows in (d).

and 556 MPa, respectively. Meanwhile, it should be noted that the elongations of the 800°C aged alloys are almost unaffected and are relatively high [6.4% (plastic strain 6.2%) and 4.4% (plastic strain 4.3%), respectively]. Apparently, a high strength and increased elongation can be achieved in the precipitation strengthening MEA by fine carbide precipitates. Figure 5b illustrates the corresponding strain hardening rate of these three MEAs as a function of the true plastic strain. For all the alloys, the strain hardening rate decreases rapidly at the initial deformation and then decreases slowly with increasing plastic strain. After aging at 800°C, the alloys exhibit an enhancement in the strain hardening rate in the late stage of the deformation, ultimately resulting in a substantial increase of the UTS. It is noted that the strain hardening rate of the 1000°C/4 h aged alloy appears to present a higher but rapidly decreasing strain hardening rate in the initial stage of deformation. It was reported that a higher hardening rate can be obtained by the abundance of rod-like particles due to their higher strain hardening rate compared to that of the granular particles, and denser dislocations can accumulate around the carbide/matrix interface; this reduces the dislocation mobility, leading to a substantial decrease in the work hardening rate.³⁰ Therefore, it is suggested that the agglomeration of strip MC carbides contributes to the higher strain hardening rate of the 1000°C/4 h aged alloy in the early deformation stage.

The strengthening mechanisms in the investigated MEAs aged at different conditions can be

described as consisting of several individual strengthening contributions according to the following equation,¹⁹ which is derived by considering that these mechanisms are operating independently, and the YS can be regarded as a simple linear combination of their individual contributions:

$$\sigma_y = \sigma_0 + \Delta\sigma_{ss} + \Delta\sigma_{ppt} + \Delta\sigma_{dis} + \Delta\sigma_{gb} \quad (1)$$

where σ_0 is the intrinsic lattice friction stress of a single crystal, and $\Delta\sigma_{ss}$, $\Delta\sigma_{ppt}$, $\Delta\sigma_{dis}$, and $\Delta\sigma_{gb}$ are the strength increases due to the solid solution, precipitates, and dislocation and grain boundaries, respectively.²¹ For the investigated alloys, their bulk composition and average grain size are the same, and they are also not subjected to the deformation and are fully annealed at high temperature, so the yield increment from the grain boundary hardening and the dislocation hardening for different states were the same; therefore, the YS difference, $\Delta\sigma_y$, is mainly comprised by $\Delta\sigma_{ss}$ and $\Delta\sigma_{ppt}$ as described by:

$$\Delta\sigma_y = \Delta\sigma_{ss} + \Delta\sigma_{ppt} \quad (2)$$

For fine MC precipitates, the lattice misfit between the precipitate and the FCC matrix was estimated to be approximately 15.6% by using the lattice constants of 0.416 nm and 0.36 nm for the MC phase and FCC matrix, respectively. This large misfit value indicates that the interface between the precipitate and the matrix is incoherent, and that the MC precipitates can strengthen the alloy by the Orowan bypass mechanism. Thus, the increase in the YS due to the Orowan mechanism can be expressed as follows:³¹

$$\Delta\sigma_p = \frac{MGb}{(\sqrt{4\pi/3f} - 2)R} \quad (3)$$

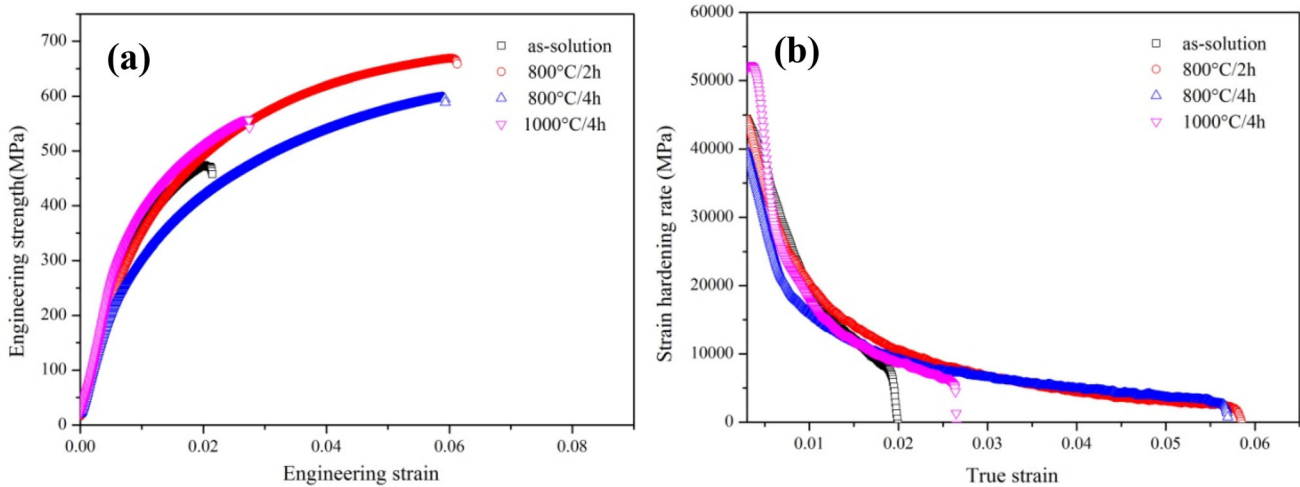


Fig. 5. Typical tensile engineering stress–strain curves (a) and strain hardening rate curves (b) of the solution-treated MEA and aged MEAs (800°C/2 h, 800°C/4 h, and 1000°C/4 h).

where M is the Taylor factor ($= 3.06$, for the FCC matrix); $G = 80$ GPa is the shear modulus of the FCC matrix;^{4,22} $b = 0.255$ nm is the Burgers vector ($= \alpha/\sqrt{2}$ for the FCC matrix, and $\alpha = 0.36$ nm is the lattice constant of the FCC);²² f is the particle volume fraction; and R is the mean size of the carbides. The precipitate size distribution for the aged alloy is presented in Fig. 6. It can be observed that the average diameter (R) of the MC precipitates in the $800^\circ\text{C}/2$ h aged alloy is measured to be approximately 24 nm, and that this value shows a slight increase (to 29 nm) as the aging time increases to 4 h. In contrast, the average precipitate diameter increases to 64 nm in the $1000^\circ\text{C}/4$ h aged alloy, which is consistent with the observations in Fig. 3g. The volume fractions (f) of the precipitates are measured to be approximately 8.32%, 5.62%, and 4.71% for the $800^\circ\text{C}/2$ h, $800^\circ\text{C}/4$ h, and $1000^\circ\text{C}/4$ h aged alloys, respectively. Substituting the obtained results into the above equation, it is found that the increase in the YS derived from the precipitation strengthening should be 510, 309, and 131 MPa for the $800^\circ\text{C}/2$ h, $800^\circ\text{C}/4$ h, and $1000^\circ\text{C}/4$ h aged alloys, respectively.

For the solid solution strengthening, the decreased strength induced by the reduced amount of interstitial carbon in the matrix during aging should not be neglected. Wang et al.³² reported that the YS increases linearly with increasing carbon concentration in an FCC-type HEA, for the increase in the YS per atomic percent of carbon (at.%) is 184 MPa/at.%C. The carbon concentration in the matrix for the $800^\circ\text{C}/2$ h aged alloy in the present work is 2.62 at.% as measured by STEM/EDX, thus the consumption of the carbon content for the total carbides (including primary carbides and secondary carbides) can be determined to be 2.38 at.% for the carbon content in the investigated alloy is 5 at.%. The primary carbides and secondary precipitates are basically similar in main constituents, but different in relative contents, and the volume fraction of primary carbides is measured to be approximately 17.76%. Thus, the consumption of the carbon content from the matrix for the $800^\circ\text{C}/2$ h aged alloy is estimated to be 0.76 at.%, leading to a reduction in the YS by 140 MPa according to the results obtained by Wang.³² Therefore, the increment of the YS due to the precipitates and

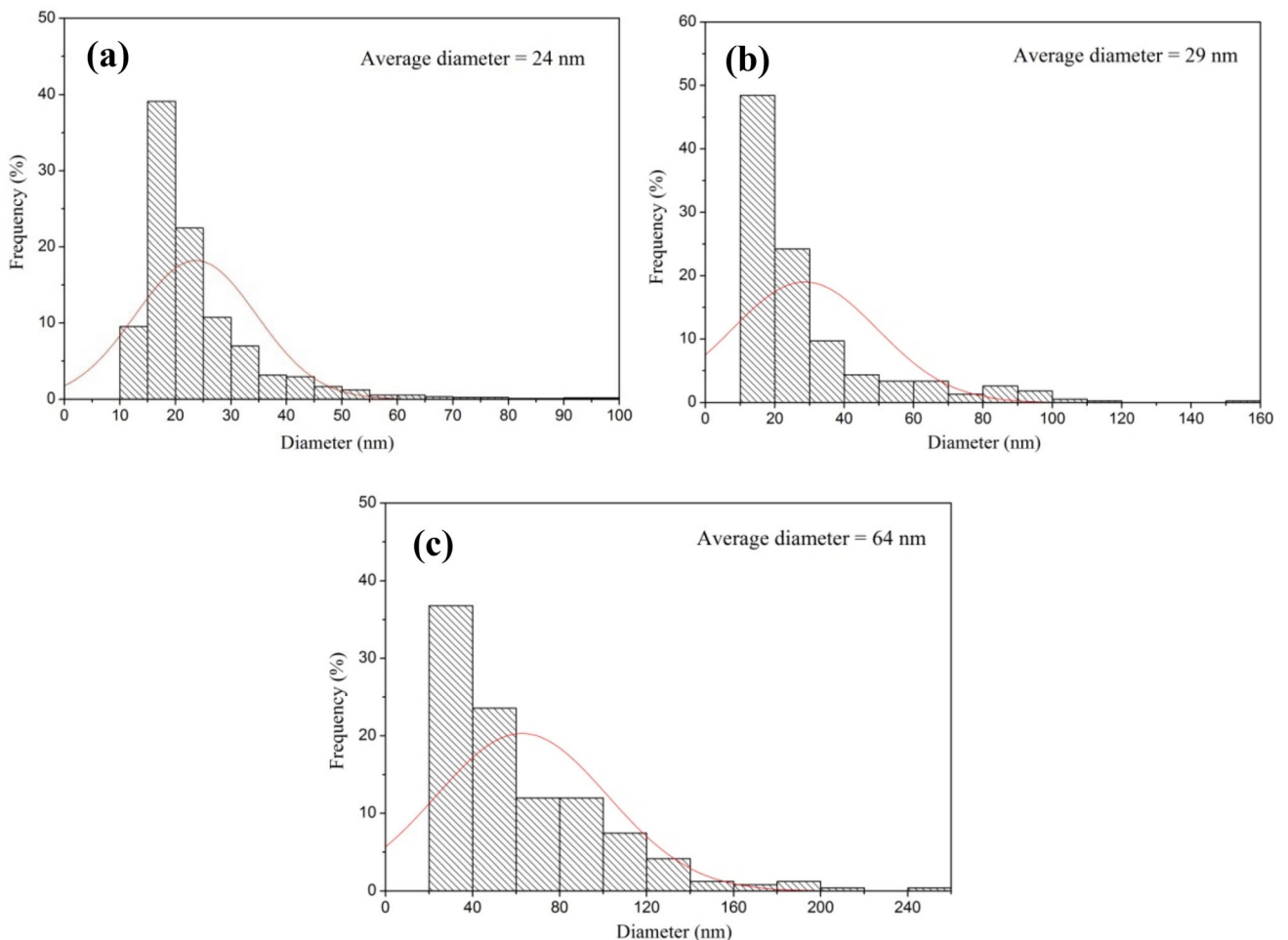


Fig. 6. Size distribution of the MC particles in the specimens aged at 800°C for 2 h (a), 4 h (b), and 1000°C for 4 h (c).

solid solution can be calculated, and the obtained values are shown in Table I. $\Delta\sigma$ decreases with increasing isothermal time and temperature, which is consistent with the observed experimental results. The simulation results of $\Delta\sigma$ for the 1000°C/4 h aged alloy with coarse precipitates are close to the experimental values. In contrast, the calculated values are approximately 120 MPa higher than their experimental counterparts for the 800°C aged samples with fine precipitates. This discrepancy can be attributed to the inappropriate parameters for the average diameter and volume fraction when the fine precipitates are not evenly distributed (as indicated by the particle distribution shown in Figs. 3 and 4). In this case, the YS increment may be controlled by the largest sparsely distributed precipitates rather than the average volume fraction. Therefore, $\Delta\sigma$ values that are lower than the calculated values can be obtained.

Typical fracture surfaces for the solution-treated MEA, 800°C/2 h aged MEA, 800°C/4 h aged MEA, and 1000°C/4 h aged MEA are shown in Fig. 7. The fracture morphology of solid solution treated alloy is characterized by many cleavage fracture facets with secondary cracks along the grain boundaries, and a small amount of tearing ridges and ductile dimples (Fig. 7a), indicating that the type of fracture is primarily brittle fracture. Under the condition of 800°C aging, a certain amount of dimples and microvoids are observed to be distributed among the cleavage facets (Fig. 7b and c), reflecting the improvement in the ductility. When the aging temperature increases to 1000°C, the fracture surface of the sample exhibits cleavage facets, dimples, and microvoids (Fig. 7d), suggesting mixed brittle and ductile fractures. It was reported that a high number density of fine granular precipitates gave rise to a superior ductility due to the good strain hardening

Table I. Experimental and simulation results for yield strength enhancement ($\Delta\sigma$ /MPa) for precipitate strengthening and solid solution

<u>Aging treatment</u>	<u>800°C/2 h</u>	<u>800°C/4 h</u>	<u>1000°C/4 h</u>
Experimental value	249	103	35
Simulated value	370	221	52

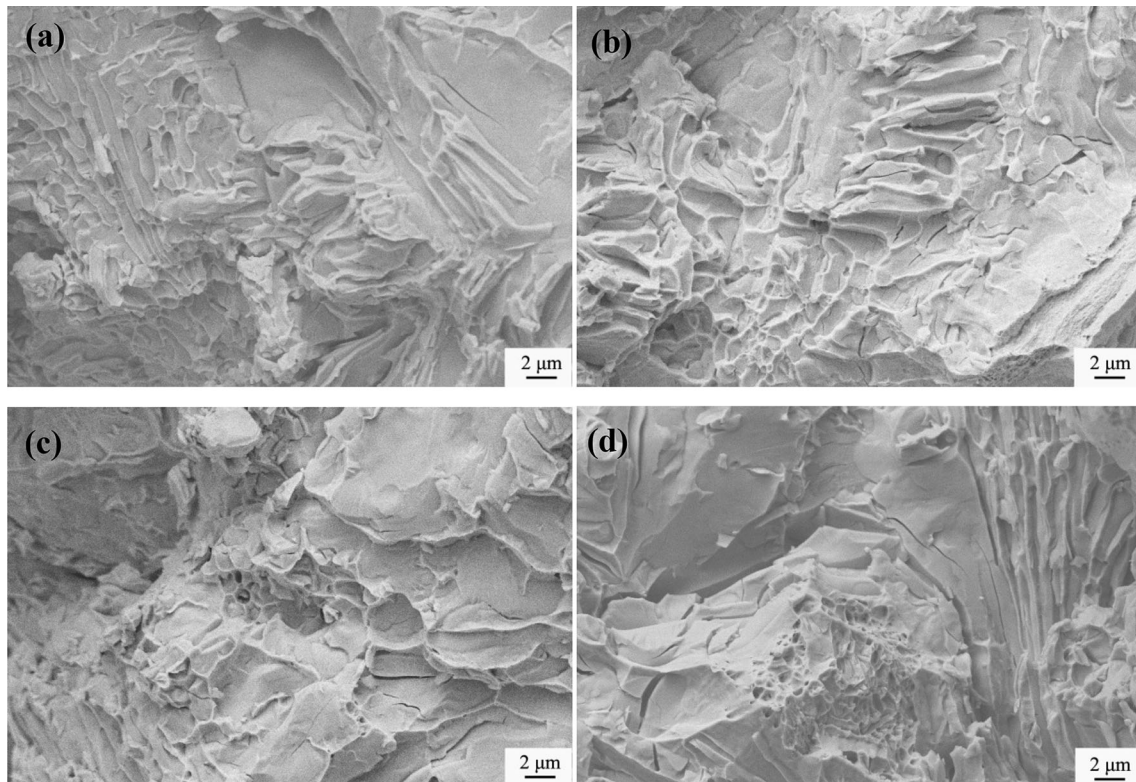


Fig. 7. Fracture surfaces of the investigated samples after tensile testing at room temperature: (a) solution-treated condition; (b) 800°C/2 h aged; (c) 800°C/4 h aged; and (d) 1000°C/4 h aged.

rate at a high strain.³⁰ In the present study, the MC phases precipitating along dislocations were observed by TEM (Fig. 4), and the nanosized MC are stable and can effectively impede dislocation movement in the FCC matrix of the alloy. Therefore, the large amount of fine MC carbides with a nanosized diameter contribute an excellent precipitation strengthening effect in the 800°C/2 h aged alloy, and the enhanced ductility may be ascribed to the dense MC phases dispersed throughout the matrix causing the dislocations to be more uniformly distributed thus reducing the stress concentration,²² giving rise to the improvement of the elongation while the UTS is substantially increased to 668 MPa (increased by 41%) compared to that of the solution-treated alloy.

CONCLUSIONS

The effect of aging at 400–1100°C on the microstructure and mechanical properties of the Fe₆₀Co₁₀Cr₁₀Ni₁₀Mo₅V₅ MEA alloy doped with 1 wt.% carbon was investigated. The precipitation behavior and strengthening effect were studied, and the main conclusions can be drawn as follows:

1. The solution-treated alloy consists of a mixture of FCC matrix, coarse M₂C, and MC carbides distributed on the grain boundaries, and minor undissolved MC precipitates inside the grains.
2. A substantial hardening effect occurred in the alloy over the temperature range of 400–1000°C, and the optimal hardness was observed at 800°C, increasing the hardness from 220 HV to 352 HV. Hardening was largely due to the precipitation of the nano-scaled MC carbide in the FCC matrix.
3. The investigated MEA aged at 800°C for 2 h has the highest YS and UTS, and an improvement in the elongation. The strengthening effect of the aged alloy has been analyzed by precipitation strengthening and solid solution strengthening.

ACKNOWLEDGEMENTS

This research was financially supported by the Scientific Research Project Fund of Jiangxi Provincial Education Department (Grant Number GJJ180479), Open Foundation of State Key Laboratory for Advanced Metals and Materials, University of Science and Technology Beijing (Grant Number 2018-Z01), Key Research and Development Project of Jiangxi Province (Grant Number 2019BBEL50016), Natural Science Foundation of Jiangxi Province (Grant Number 20202BABL204010), and Program of the University Students' Innovation and Pioneering (Grant No. DC2019-034).

CONFLICT OF INTEREST

The authors declare that they have no conflict of interest.

SUPPLEMENTARY MATERIAL

The online version of this article (<https://doi.org/10.1007/s11837-020-04528-3>) contains supplementary material, which is available to authorized users.

REFERENCES

1. J.W. Yeh, S.K. Chen, S.J. Lin, J.Y. Gan, T.S. Chin, T.T. Shun, C.H. Tsau, and S.Y. Chang, *Adv. Eng. Mater.* 6, 299 (2004).
2. B. Cantor, I. Chang, P. Knight, and A. Vincent, *Mater. Sci. Eng.*, A 375–377, 213 (2004).
3. T. Yang, Y.L. Zhao, Y. Tong, Z.B. Jiao, J. Wei, J.X. Cai, X.D. Han, D. Chen, A. Hu, J.J. Kai, K. Lu, Y. Liu, and C.T. Liu, *Science* 362, 933 (2018).
4. Z. Wu, H. Bei, G.M. Pharr, and E.P. George, *Acta Mater.* 81, 428 (2014).
5. G. Laplanche, A. Kostka, C. Reinhart, J. Hunfeld, G. Egeler, and E.P. George, *Acta Mater.* 128, 292 (2017).
6. J.Y. He, C. Zhu, D.Q. Zhou, W.H. Liu, T.G. Nieh, and Z.P. Lu, *Intermetallics* 55, 9 (2014).
7. G. Laplanche, P. Gadaud, C. Bärsch, K. Demtröder, C. Reinhart, J. Schreuer, and E.P. George, *J. Alloys Compd.* 746, 244 (2018).
8. W.H. Liu, Y. Wu, J.Y. He, T.G. Nieh, and Z.P. Lu, *Scr. Mater.* 68, 526 (2013).
9. O.N. Senkov, J.M. Scott, S.V. Senkova, D.B. Miracle, and C.F. Woodward, *J. Alloys Compd.* 509, 6043 (2011).
10. D. Ikeuchi, D.J. King, K.J. Laws, A.J. Knowles, R.D. Aughterson, G.R. Lumpkin, and E.G. Obbard, *Scr. Mater.* 158, 141 (2019).
11. Y. Zou, S. Maiti, W. Steurer, and R. Spolenak, *Acta Mater.* 65, 85 (2014).
12. H. Huang, Y. Wu, J. He, H. Wang, X. Liu, K. An, W. Wu, and Z. Lu, *Adv. Mater.* 29, 1701678 (2017).
13. N.D. Stepanov, N.Y. Yurchenko, S.V. Zherebtsov, M.A. Tikhonovsky, and G.A. Salishchev, *Mater. Lett.* 211, 87 (2018).
14. M. Feuerbacher, M. Heidelmann, and C. Thomas, *Mater. Res. Lett.* 3, 1 (2015).
15. A. Takeuchi, K. Amiya, T. Wada, K. Yubuta, and W. Zhang, *JOM* 66, 1984 (2014).
16. Y.J. Zhao, J.W. Qiao, S.G. Ma, M.C. Gao, H.J. Yang, M.W. Chen, and Y. Zhang, *Mater. Des.* 96, 10 (2016).
17. B. Gludovatz, A. Hohenwarter, D. Catoor, E.H. Chang, E.P. George, and R.O. Ritchie, *Science* 345, 1153 (2014).
18. W.H. Liu, Z.P. Lu, J.Y. He, J.H. Luan, Z.J. Wang, B. Liu, Y. Liu, M.W. Chen, and C.T. Liu, *Acta Mater.* 116, 332 (2016).
19. J.Y. He, H. Wang, H.L. Huang, X.D. Xu, M.W. Chen, Y. Wu, X.J. Liu, T.G. Nieh, K. An, and Z.P. Lu, *Acta Mater.* 102, 187 (2016).
20. W.H. Liu, J.Y. He, H.L. Huang, H. Wang, Z.P. Lu, and C.T. Liu, *Intermetallics* 60, 1 (2015).
21. R. Zhou, Y. Liu, B. Liu, J. Li, and Q.H. Fang, *Intermetallics* 106, 20 (2019).
22. N. Gao, D.H. Lu, Y.Y. Zhao, X.W. Liu, G.H. Liu, Y. Wu, G. Liu, Z.T. Fan, Z.P. Lu, and E.P. George, *J. Alloys Compd.* 792, 1028 (2019).
23. C. Scott, B. Remy, J.L. Collet, A. Cael, C. Bao, F. Danoix, B. Malard, and C. Curfse, *Int. J. Mater. Res.* 102, 538 (2011).
24. R.A. Mesquita, C.A. Barbosa, E. Morales, and H.J. Kestenbach, *Metall. Mater. Trans. A* 42, 461 (2011).
25. H. Wang, L. Hou, J. Zhang, L. Lu, H. Cui, and J. Zhang, *Mater. Charact.* 106, 245 (2015).
26. M.J. Yao, K.G. Pradeep, C.C. Tasan, and D. Raabe, *Scr. Mater.* 72–73, 5 (2014).
27. Z. Li, K.G. Pradeep, Y. Deng, D. Raabe, and C.C. Tasan, *Nature* 534, 227 (2016).
28. J.W. Bae, J.B. Seol, J. Moon, S.S. Sohn, M.J. Jang, H.Y. Um, B. Lee, and H.S. Kim, *Acta Mater.* 161, 388 (2018).

29. P. Ou, H. Xing, and J. Sun, *Metall. Mater. Trans. A* 46, 1 (2015).
30. X.F. Zhou, W.T. Li, H.B. Jiang, F. Fang, Y.Y. Tu, and J.Q. Jiang, *Metall. Mater. Trans. A* 50, 1682 (2019).
31. Z.B. Jiao, J.H. Luan, Z.W. Zhang, M.K. Miller, and C.T. Liu, *Scr. Mater.* 87, 45 (2014).
32. Z.W. Wang, I. Baker, Z.H. Cai, S. Chen, J.D. Poplawsky, and W. Guo, *Acta Mater.* 120, 228 (2016).

Publisher's Note Springer Nature remains neutral with regard to jurisdictional claims in published maps and institutional affiliations.